Modeling the Lunar Wake Response to a CME Using a Hybrid PIC Model

Anthony P. Rasca[1] , Shahab Fatemi[2], and William M. Farrell[1]

[1] Solar System Exploration Division, NASA/Goddard Space Flight Center, Greenbelt, MD, USA; anthony.p.rasca@nasa.gov
[2] Department of Physics, Umeå University, Sweden

Abstract

In the solar wind, a low-density wake region forms downstream of the nightside lunar surface. In this study, we use a series of 3D hybrid particle-in-cell simulations to model the response of the lunar wake to a passing coronal mass ejection (CME). Average plasma parameters are derived from the Wind spacecraft located at 1 au during three distinct phases of a passing halo (Earth-directed) CME on 2015 June 22. Each set of plasma parameters, representing the shock/plasma sheath, a magnetic cloud, and plasma conditions we call the mid-CME phase, are used as the time-static upstream boundary conditions for three separate simulations. These simulation results are then compared with results that use nominal solar wind conditions. Results show a shortened plasma void compared to nominal conditions and a distinctive rarefaction cone originating from the terminator during the CME's plasma sheath phase, while a highly elongated plasma void reforms during the magnetic cloud and mid-CME phases. Developments of electric and magnetic field intensification are also observed during the plasma sheath phase along the central wake, while electrostatic turbulence dominates along the plasma void boundaries and 2–3 lunar radii R_M downstream in the central wake during the magnetic cloud and mid-CME phases. The simulations demonstrate that the lunar wake responds in a dynamic way with the changes in the upstream solar wind during a CME.

Unified Astronomy Thesaurus concepts: Solar coronal mass ejections (310); Space plasmas (1544); Theoretical models (2107); The Moon (1692)

1. Introduction

As one can imagine, the Moon is an obstacle in the solar wind plasma flow. Observations by the Acceleration, Reconnection, Turbulence, and Electrodynamics of the Moon's Interaction with the Sun (THEMIS-ARTEMIS, an extension of the Time History of Events and Macroscale Interactions during Substorms mission) spacecraft indicate that associated plasma disturbances create strong electric fields just downstream of the terminator and the formation of an extended wake structure that is gradually refilled by electrons and ions downstream (Zhang et al. 2014; Xu et al. 2019). Numerous particle-in-cell (PIC) and hybrid PIC simulations of the steady flow past the Moon also reveal the presence of these downstream disturbances (Farrell et al. 1998; Birch & Chapman 2001; Wang et al. 2011; Fatemi et al. 2012, 2013; Holmström et al. 2012; Poppe et al. 2014; Rasca et al. 2021). There are also several modeling studies focusing on the lunar wake structure under nominal solar wind conditions using MHD descriptions (Spreiter et al. 1970; Cui & Lei 2008; Xie et al. 2013; Michel 2014) as well as particle (Farrell et al. 1998; Birch & Chapman 2001; Nakagawa 2013) and hybrid PIC models (Wang et al. 2011; Fatemi et al. 2012, 2013; Holmström et al. 2012; Vernisse et al. 2013; Poppe et al. 2014).

While the solar wind at 1 au is often a steady radial flow, it exhibits variability during the solar cycle and passing extreme events such as Earth-directed (halo) coronal mass ejections (CMEs), which are commonly associated with geomagnetic storms (Richardson et al. 2001). CMEs are formed when hot dense plasma is released and accelerated from the solar corona. While acceleration of the plasma varies, it can reach speeds

exceeding $500\,\mathrm{km\,s^{-1}}$ at 1 au, with some events surpassing $1000\,\mathrm{km\,s^{-1}}$ (Richardson & Cane 2010; Compagnino et al. 2017). Halo CMEs can suddenly and substantially alter the plasma-flow environment at the Moon and first arrive in the form of a plasma shock, immediately followed by an accelerated plasma sheath consisting of warm dense plasma (Farrell et al. 2012). Lunar exposure to the plasma sheath can last more than 10 hr and is followed by a reduction in ion temperature and velocity. Following the plasma sheath, magnetic cloud features are sometimes observed, caused by flux ropes or other coherent magnetic structures characterized by rotations in the magnetic field that can last up to multiple days before rotating to their previous state (Burlaga et al. 1981). Multiple phases make a passing CME a highly dynamic plasma event—often lasting more than a day—and an important focus for assessing the response of the lunar plasma environment.

Several studies have already addressed the near-surface lunar wake environment and effects of CMEs and solar energetic particle (SEP) events at the lunar surface. An example is the solar-storm/lunar-atmosphere model (SSLAM) study (Farrell et al. 2012; Zimmerman et al. 2012), which looked at a sample CME's effects on the lunar plasma environment during its 1998 May 1–4 passage and showed enhanced surface particle release (via sputtering/reflection) on the dayside and enhanced electric fields/potentials in wakes and shadowed craters. Additional effects occur at the global plasma wake on the lunar nightside, as solar wind particles try to fill the resulting plasma void, detected by spacecraft such as Wind, Lunar Prospector (LP), and more recently, THEMIS-ARTEMIS, during transits through the lunar wake (Halekas et al. 2005, 2011; Tao et al. 2012; Zhang et al. 2012, 2014; Xu et al. 2019).

At full lunar scale, both fluid and kinetic processes play an important role in the wake refilling processes and are influenced
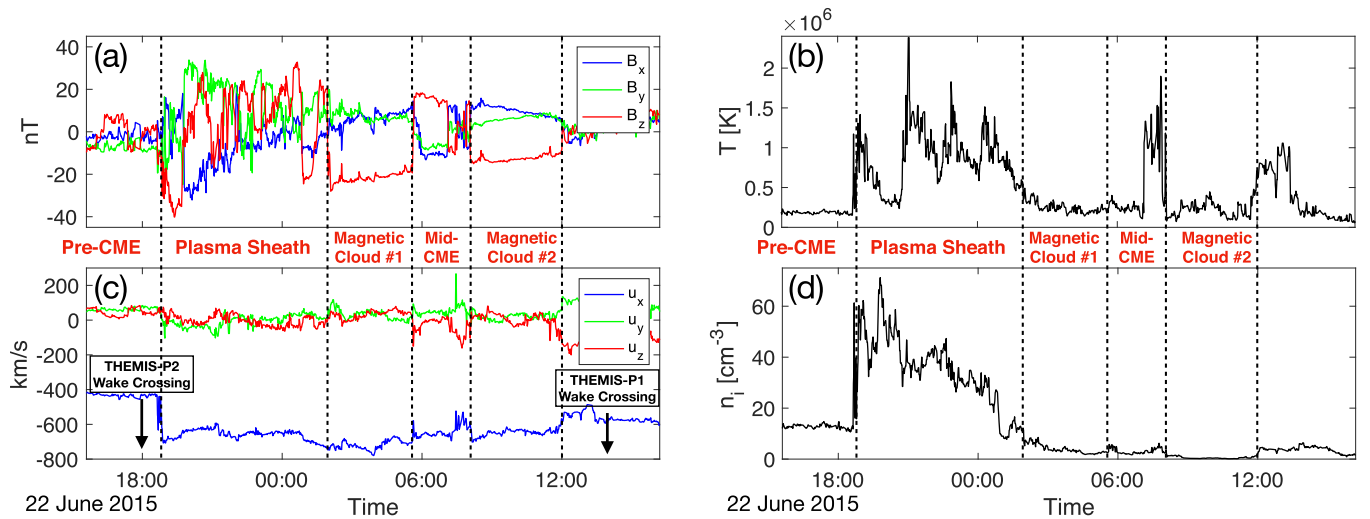
Figure 1. Plasma parameters measured by the Wind spacecraft during the passing CME on 2015 June 22–23. Displayed are (a) the magnetic field components, (b) ion temperature, (c) velocity components, and (d) ion density.

heavily by the interplanetary magnetic field (IMF) orientation with respect to the wake boundary normal (Holmström et al. 2012). As a result of this spatial scale gap between MHD and PIC models, we utilize a third code that can help accurately and smoothly feed critical CME plasma parameters from a large-scale heliosphere domain to small-scale surface/near-surface simulations. In this paper, we use a hybrid PIC code as an intermediate model between fluid and particle descriptions to model the lunar wake during several phases of a CME.

We will begin by describing the CME event and upstream plasma parameters used in our study (including nominal solar wind conditions) in the following section. A thorough description of the hybrid PIC code will be made in Section 3, followed by our lunar wake results. We will conclude with a discussion and conclusions of our results.

2. Observational Data

A one-week period beginning on 2015 June 18 displayed significant solar activity with the occurrence of several M-class flares originating from AR 12371 (Gopalswamy et al. 2018). More significantly, a number of these flares produced halo CMEs, including a CME on 2015 June 21 that caused a large geomagnetic storm the following day. We choose this event to use in our study due to the wealth of high-quality observations of the CME. This event is well-studied for its direct impact on the Earth's magnetosphere as a thorough Sun-to-Earth analysis (Gopalswamy et al. 2018) and through comprehensive data analyses and MHD modeling (Astafyeva et al. 2016; Reiff et al. 2016; Piersanti et al. 2017). Additional understanding of the CME's effects on the lunar environment will help provide a complete picture of its influence on the entire Earth–Moon system.

The CME was observed near 1 au by the Wind spacecraft in the solar wind at the L_1 Lagrangian point. Figure 1 shows CME plasma and magnetic field measurements by Wind during a 24 hr period encompassing most of the CME passage. The magnetic field and velocity components are plotted on the left and the ion temperature and ion density on the right. Magnetic field and velocity components are provided in the SSE coordinate system, where $+x$ points toward the Sun, $+z$ is perpendicular to the ecliptic in the direction of ecliptic north,

and $+y$ completes the right-hand frame. The CME shock front was first detected by Wind near 1 au around 18:30 UT on 2015 June 22 and the CME reached the Moon less than 30 minutes later, where it was viewed by THEMIS-ARTEMIS as a variable plasma sheath followed by the two magnetic clouds with little to no separation. Pre-CME conditions prior to this time are not typical of nominal solar wind conditions due to the northern edge of a CME passing by the Earth the previous day (Gopalswamy et al. 2018), as the CME of this study was part of a series of flare-induced storms that were emitted from the Sun during the one-week period. The nominal solar wind at 1 au has a typical ion density and temperature of $\sim5\,\mathrm{cm}^{-3}$ and $\sim10^5$ K, respectively, and an IMF forming a Parker spiral in the xy-plane $45°$ from the $-x$-axis. During the pre-CME period in Figure 1, the ion density and temperature are higher than the nominal conditions and the IMF has a non-negligible z-component, but these are near enough to typical conditions for our study.

Different phases of the passing CME in Figure 1 are separated by vertical dashed lines. On the far left, we have the pre-CME conditions, where the solar wind has not yet returned to nominal conditions following the previous CME. The seven hours following the first dashed line form the plasma sheath phase, characterized by an accelerated hot and dense plasma flow and a highly variable magnetic field. This is followed by two magnetic cloud features that were noted by Gopalswamy et al. (2018) and Piersanti et al. (2017), with durations bounded by large and sudden reversals in B_z and separated by warmer, sparse post-sheath plasma we refer to as mid-CME conditions. The magnetic clouds are transients characterized by strong magnetic field rotations nearly $180°$ from a nominal configuration and by drops in ion temperature and density. Changes in the magnetic field at the boundaries of the magnetic cloud phases are very clear and uncharacteristically sudden in this plot, with each magnetic cloud lasting about four hours. Previous studies by Holmström et al. (2012) using hybrid PIC simulations show that the lunar wake structure is sensitive to magnetic field orientation, which emphasizes the importance of understanding how the lunar wake environment reacts to the different phases.

This CME event was also observed by the THEMIS-ARTEMIS P1 and P2 spacecraft in lunar orbit and therefore in much closer proximity to the Moon than Wind, though neither

spacecraft transited the lunar wake in the 18 hr following the CME shock. The P2 spacecraft does complete a lunar wake crossing around 18:00 UT on 2015 June 22—shortly before the CME shock—and the next THEMIS-ARTEMIS wake crossing is not until 14:00 UT the following day by P1. Unfortunately, neither of these wake crossings (indicated in Figure 1) occur during the outlined CME phases and cannot be compared with wake models in this study.

We choose Wind as a single stationary—with respect to the Earth—source of measurements for upstream solar wind and CME plasma conditions near 1 au. In this study, THEMIS-ARTEMIS could provide an alternative source of plasma measurements outside the lunar wake, though they do not observe a mid-CME phase separating the two magnetic clouds. It is possible this mid-CME feature changed during its passage to the Moon or was only detectable along the Sun-to-Wind axis. Lunar wake model results for the mid-CME phase can therefore be considered potential signatures from future events passing directly by the Moon.

Plasma conditions during each phase—especially during the two magnetic clouds phases—are relatively stable without major fluctuations for tens of minutes to an hour. We thus use mean values during the pre-CME, plasma sheath, mid-CME, and first magnetic cloud phases in four separate simulations as time-static upstream boundary conditions. The second magnetic cloud is omitted from our set of simulations, as the similar plasma conditions and magnetic field configuration to the first magnetic cloud would make it redundant.

3. Model

Our set of lunar wake simulations are run using the Amitis code developed by Fatemi et al. (2017). Amitis is a GPU-based, 3D hybrid model that describes the plasma interaction of planetary bodies with ambient plasmas and differs from a purely fluid model by treating the electrons as a massless fluid and ions as particles. The electric fields associated with plasma pressure gradients are quantified as well. These fields become important when considering the plasma expansion process into a trailing void or wake region. Thus, this model is ideal for examining the solar wind plasma interaction with the Moon and for the formation of the trailing wake region that extends many lunar radii downstream. Numerous studies have used Amitis to model solar wind interactions with planetary bodies ranging in size from asteroids to Mercury (Fatemi et al. 2017, 2018, 2020; Fatemi & Poppe 2018; Fuqua Haviland et al. 2019; Garrick-Bethell et al. 2019; Poppe 2019; Rasca et al. 2021).

Amitis runs were performed using four different sets of time-dependent upstream boundary conditions, each running until a steady-state is reached ($\sim$100 s), determined when there is no longer considerable changes in time in the electric and magnetic fields, plasma density, and velocity. The Moon is assumed to be a nonconductive body with resistivity $10^{-7}\,\mathrm{S\,m^{-1}}$ and its surface a perfect plasma absorber (solar wind protons impacting the surface of the Moon are removed from the simulations). All runs are performed with a computational domain on a Cartesian grid oriented using the SSE coordinate system and measuring $[x_{\min}, x_{\max}] \times [y_{\min}, y_{\max}] \times [z_{\min}, z_{\max}] = [-6.9, 3.4] \times [-4.6, 4.6] \times [-4.6, 4.6]\,R_M$, where $R_M = 1737$ km is a lunar radius, the $+x$-axis points toward the Sun, and the Moon is at the origin in the hybrid simulation box. Each cubic grid cell measures 100 km across, creating a $180 \times 160 \times 160$ cell grid. Solar wind particles are injected in the $-x$ direction from the inflow

Table 1
Upstream Plasma Parameters for Hybrid Simulations

	Pre-CME	Plasma Sheath	Magnetic Cloud	Mid-CME
n_{i0} (cm^{-3})	13	39	4	3
T_0 (K)	2×10^5	9×10^5	2.5×10^5	5×10^5
$|u_{x0}|$ (km s^{-1})	440	650	720	650
$\boldsymbol{B_0}$ (nT)	[−1.8, −5.8, −2.7]	[−6.4, 11.2, 4.2]	[6.3, 7.3, −21.5]	[−3.9, −3.4, 9.7]
M_A	10.9	13.7	2.8	4.7
M_C	8.4	5.8	12.3	7.8
β	2.0	6.6	0.1	0.4

boundary (i.e., $x = +3.4\,R_M$) and removed from the outflow boundary ($x = -6.9\,R_M$). The simulations are periodic along other dimensions.

Upstream plasma parameters for each run are shown in Table 1, along with the Alfvénic and sonic Mach numbers M_A and M_C, respectively. The plasma parameters of the various event phases are selected to emphasize the sudden changes in conditions immediately following CME arrival. The plasma is assumed to consist only of populations of solar wind protons and electrons and the upwind plasma has an assumed flow purely in the $-x$ direction. Pre-CME conditions, as indicated earlier, are not representative of typical solar wind conditions at 1 au. The higher density is representative of a transitionary period between a mid-CME ($\sim$10$\times$ that of solar wind, Farrell et al. 2012) and the nominal solar wind. Of the four phases in Table 1, the plasma sheath exhibits the highest density and temperature, while the magnetic cloud delivers plasma at the highest mean velocity and magnetic field strength while also having a very low total plasma β. We must also note the variable magnetic field and plasma parameters during the plasma sheath phase that are averaged to get the corresponding mean values in Table 1. While the mean parameters may not match the plasma conditions during certain portions of this phase, they represent the general hot and dense characteristics of a CME plasma sheath and exceed the proton temperature and density parameters of the 1998 May 1–4 CME studied by Farrell et al. (2012) by a factor of two.

4. Results

Figure 2 shows the initial pre-CME configuration of the lunar wake generated by the Amitis code using parameters in Table 1 in the coordinate frame described above. Shown are the plasma density (top left) normalized by the upstream density n_{i0} in Table 1, ion velocity components normal to u_x (top right), magnetic field magnitude (bottom left) normalized by the upstream magnetic field magnitude B_0, and electric field vectors and magnitude (bottom right). Each property is shown as cuts in the xy- and xz-planes. A clear and distinct void with compressed magnetic and electric fields forms downstream from the lunar nightside. This downstream void is much shorter than that modeled by Holmström et al. (2012) with nominal solar wind conditions and a 45° Parker spiral IMF, with wake refilling aided by the higher plasma temperatures enhancing the plasma expansion process (Fatemi 2014). The B_y-dominated magnetic field aids by accelerating ions into the wake along field lines parallel to the boundary normal (a kinetic process). This process is illustrated by u_y in the xy-plane and u_z in the xz-plane, where the intense red and blue regions represent two separate ion streams accelerating into the wake opposite each

Pre-CME

Ion Density

Ion Velocity Components

B-Field Magnitude
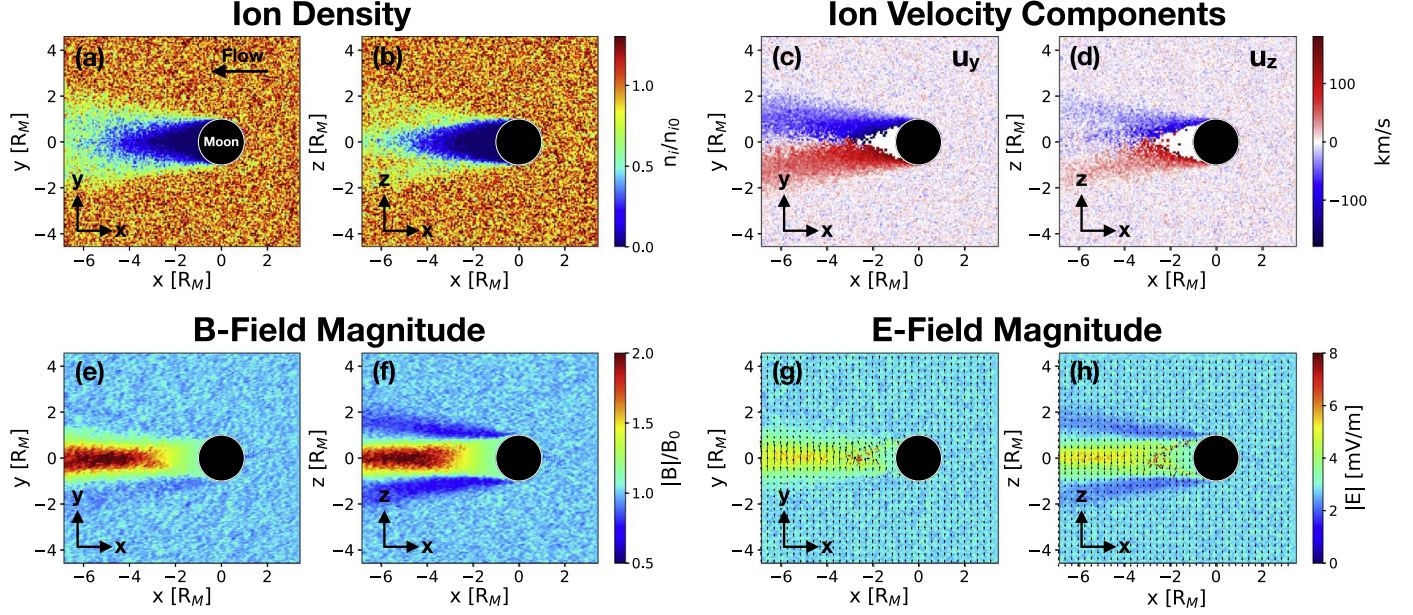

E-Field Magnitude

Figure 2. Amitis results using pre-CME plasma conditions (Table 1). Results are shown in the xy- and xz-planes for the normalized ion density (top left), ion velocity components (top right), normalized magnetic field magnitude (bottom left), and electric field magnitude with the electric field overlaid (lower right).

other and combining along the x-axis from around $-2\ R_M$ to $-4\ R_M$. In the xz-plane, a faint rarefaction region is evident in the ion density, characterized by apparent narrow streams of lower ion density originating from the north and south terminators. The lack of a well-defined rarefaction boundary relative to wake results by Holmström et al. (2012) is due to nonzero magnetic field components upstream (Table 1), which breaks the cylindrical symmetry of the wake.

The Amitis code is run three more times, with plasma sheath, magnetic cloud, and mid-CME upstream parameters listed in Table 1. Results are shown in Figures 3 and 4 in the same xy- and xz-planes as Figure 2. The plasma sheath generates the shortest plasma wake, which we attribute to the high plasma temperature accelerating plasma expansion into the void. This phase is accompanied by ions flowing rapidly into the wake along the very distinct rarefaction region (see Figure 3, top row). The plasma density rarefaction region completely disappears during the magnetic cloud phase (see Figures 3(e)–(f)). During this time, the upstream ion temperature decreases and results show an elongated plasma wake. Lower plasma temperatures reduce expansion into the nightside void, possibly explaining a diminished rarefaction response. The low β during this phase also indicates that the magnetic field pressure dominates over the particle pressure during this phase. A similarly elongated wake forms during the mid-CME phase (Figures 3(i)–(j)), but a very faint rarefaction region appears in the xy-plane (indicated).

Figure 4 shows the normalized magnetic field magnitude (left) and electric field vectors and magnitude (right) during the three CME phases shown in Figure 3. During the plasma sheath phase, the compressed magnetic and electric field structures in the lunar wake resemble scaled versions of the pre-CME wake structure in Figures 2(g)–(h). In the xy-plane during the mid-CME, the magnetic and electric field magnitude plots show features resembling a Mach cone boundary and rarefaction region (blue streams in each plot) angled about $15°$ with respect

to the lunar shadow boundary (optical wake). Another notable feature in the magnetic field during the magnetic cloud phase is a generally more enhanced northern ($+z$) region within the cone boundary, with the enhancement extending from the lunar nightside surface in the $-x$, $+z$-direction instead of along the central wake. The lack of an ion sonic rarefaction wave and the formation of a magnetic Mach cone feature suggests that wake disturbance in the low-β case is significantly different than the high plasma pressure cases.

Figures 4(g)–(h) show significant electrostatic turbulence further downstream where the two ion streams combine. Such phenomena have been observed associated with unstable ion beams in the central lunar wake and in the terrestrial bow shock (Farrell et al. 1997; Bale et al. 1998). While some electrostatic turbulence is present during the other phases, it persists along the void boundary and reaches $-6\ R_M$ in the central wake. Figure 5 provides a different view of the electrostatic turbulence across the wake, along $x = -2\ R_M$ and $x = -5\ R_M$ in the xy- (left) and xz-planes (right). The top panels show E_x along these two cuts, while the bottom panels show E_y along cuts in the xy-plane and E_z along cuts in the xz-plane with the corresponding ambient field components subtracted. The cuts in the xy- and xz-planes are shown in Figures 4(g)–(h) as black vertical lines. Along $x = -2\ R_M$ the void boundaries are located about $0.5\ R_M$ from the x-axis. Inside the wake near the lunar nightside (blue), significant turbulence and wave activity are limited to the the void boundaries where bipolar spikes in the electric field components can reach magnitudes of nearly 4 mV m^{-1}. Further downstream in the wake (red), electrostatic wave activity increases in amplitude and extends from the optical wake into the center of the wake. Here, the dual ion streams are combining to form the downstream plasma flow in the wake, generating the wide turbulent region in Figures 4(g)–(h) as they slow down. This process has previously been illustrated by Farrell et al. (1997) for the central lunar wake.
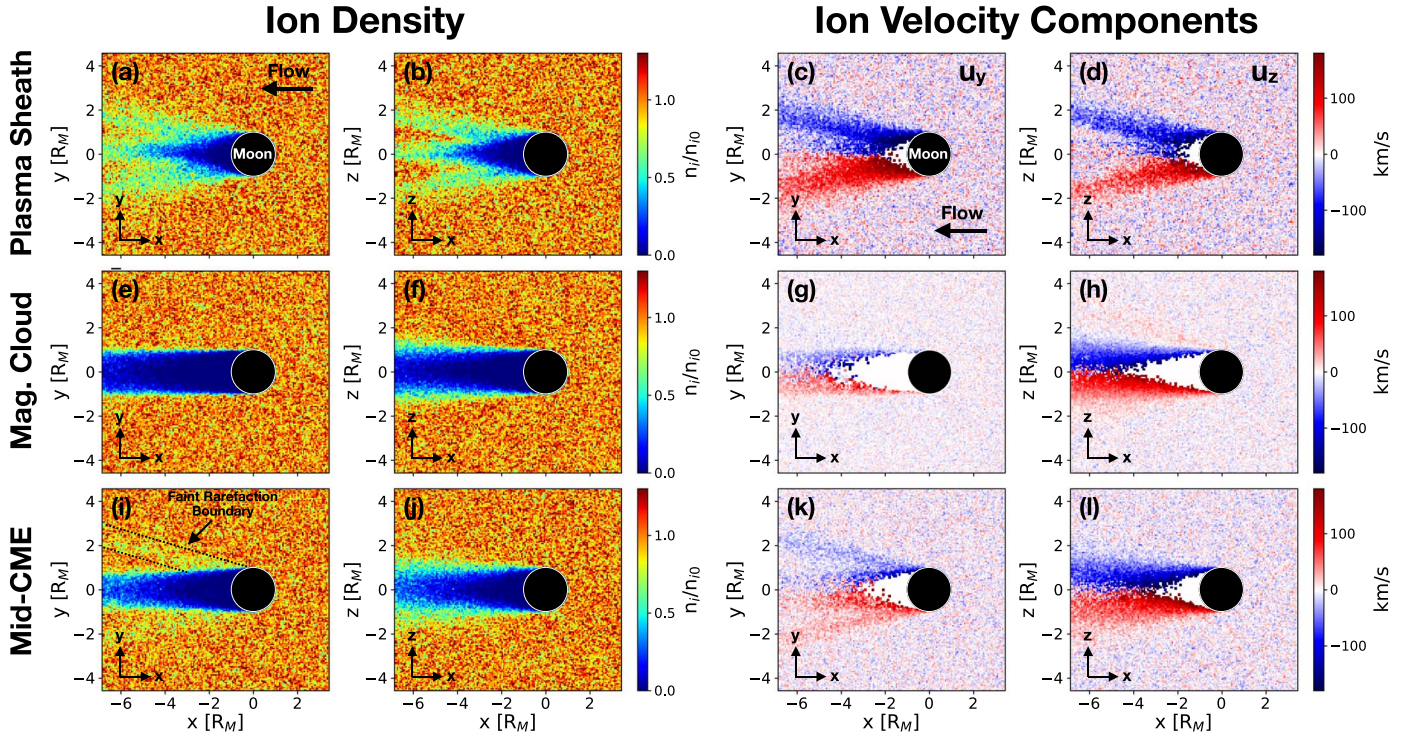
Figure 3. Amitis results using upstream plasma parameters from three different phases during the 2015 June 22 CME (Table 1). Results are shown in the *xy*- and *xz*-planes for the normalized ion density (left) and ion velocity components (right) during the plasma sheath (top row), magnetic cloud (middle row), and mid-CME (bottom row).
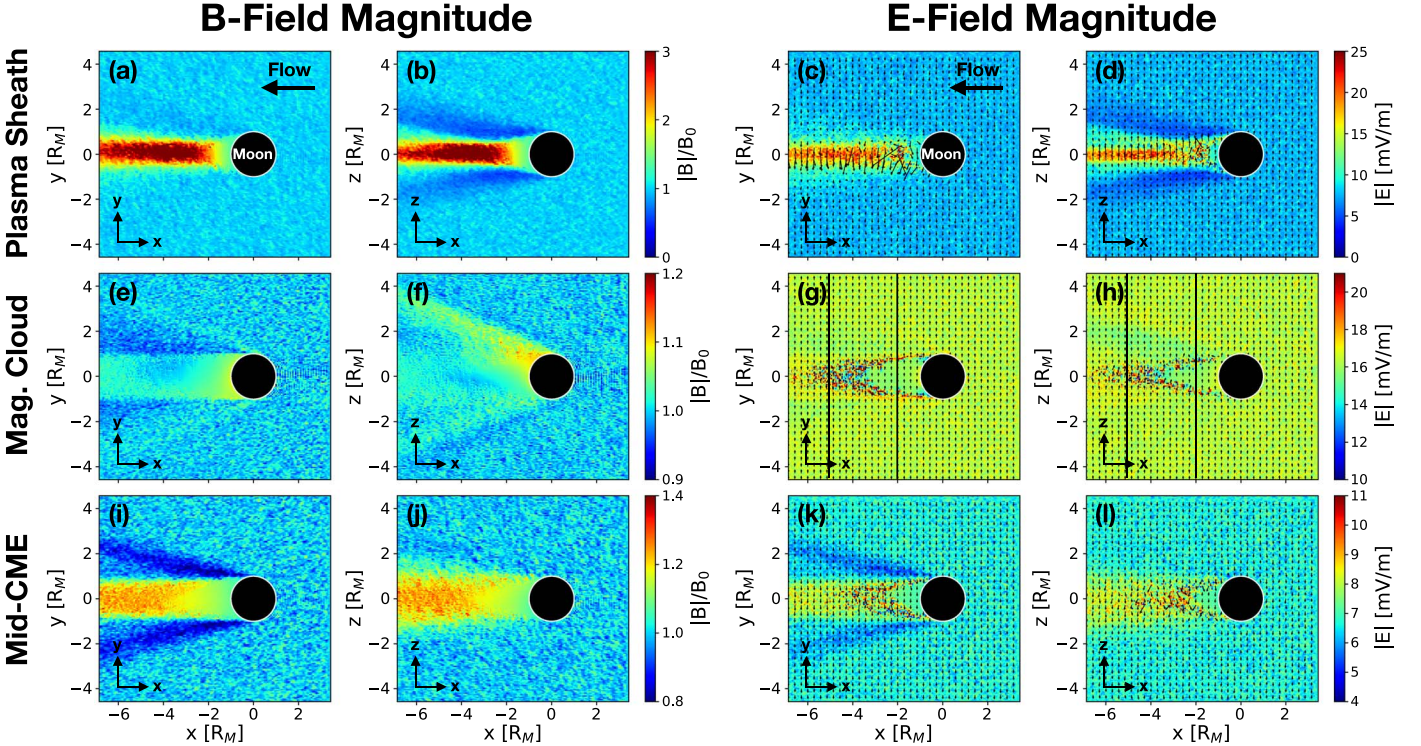

Figure 4. Amitis results using upstream plasma parameters from three different phases during the 2015 June 22 CME (Table 1). Results are shown in the *xy*- and *xz*-planes for the normalized magnetic field magnitude (left) and electric field magnitude with the electric field overlaid (right) during the plasma sheath (top row), magnetic cloud (middle row), and mid-CME (bottom row).

5. Discussion and Conclusions

Examining different phases of a CME using hybrid simulations highlights changes the lunar wake can undergo over the course of hours. In most simulations, a wake structure consisting of a rarefaction region, recompression region, and plasma void are evident in either the plasma density or the
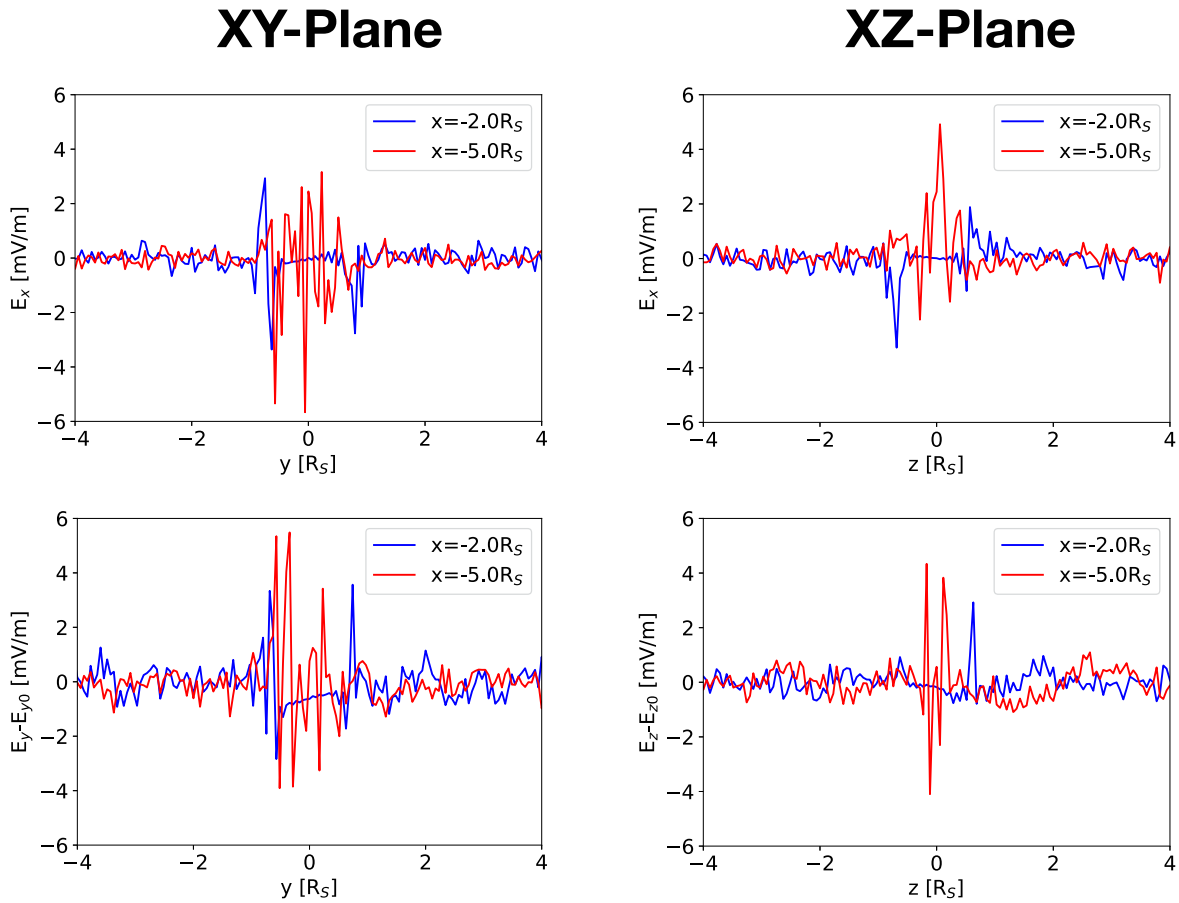
Figure 5. Electric field components along $x = -2\,R_M$ (blue) and $x = -5\,R_M$ (red) in the xy- (left) and xz- (right) planes. E_x and E_y and shown for the xy-plane, while E_x and E_z are shown for the xz-plane and have the corresponding ambient field components subtracted.

magnetic field magnitude. In particular, strong rarefaction and recompression regions stand out in the plasma density during the plasma sheath phase, where the wake is quickly refilled with ions. This is a familiar picture of the lunar wake and has been developed and modeled in several studies (Wolf 1968; Holmström et al. 2012; Fatemi et al. 2013).

The maximum magnetic field strength in the wake as a function of β generally agrees with a relation derived by Fatemi (2014), $B_{wake} = B_{sw}\sqrt{1 + \beta}$ for an IMF perfectly parallel to the solar wind flow. This relation stems from a 1D fluid model for the pressure balance that forms between a stationary plasma expanding into the void perpendicular to B_{sw} and the magnetic pressure inside the void. Even as a simplified model, the relation is supported by THEMIS-ARTEMIS observations during wake crossings with a near-parallel upstream magnetic field (Poppe et al. 2014). However, during each phase in Table 1 the upstream magnetic fields have a large component perpendicular to the flow direction, causing the void to fill in further upstream than with a parallel IMF. For this reason the relation here may not hold exactly, but the magnetic field strength in the wake relative to upstream conditions (Figures 2 and 4) increases with β in Table 1.

Of our results, the magnetic cloud phase stands out the most as a unique plasma structure forms in the wake. This is evident by a void extending the furthest downstream (see Figures 3(g)–(h)), with an extended turbulent region of counter-streaming ions. This phase also has the lowest upstream Alfvén Mach number and plasma β, while also possessing the highest

upstream sonic Mach number of $M_C = 12.3$, compared to 8.4 and 5.8 for the pre-CME and plasma sheath phases, respectively.

The magnetic cloud phase particularly stands out with respect to its magnetic field and ion sonic wake structure. An ion sonic wake structure typically consists of an outer Mach cone bounding rarefaction and recompression regions outside the void boundaries (illustrated in Figure 4 of Fatemi et al. 2013) and a compressed magnetic field in the central wake. This structure is apparent in the ion density and magnetic field magnitude plots for the pre-CME (Figure 2) and plasma sheath (Figures 3–4) phases. However, the magnetic cloud phase departs from this structure. A plasma rarefaction region is not evident during the magnetic cloud phase (see Figure 3). Instead, a disturbance is formed in the magnetic field (Figure 4, middle row). In Figures 4(e)–(f), the outer boundary of this disturbance resembles a Mach cone flared about 24° from the optical wake boundary. Though this boundary resembles Mach cones in the plasma density during the pre-CME and plasma sheath phases, the high ion sonic Mach number during the magnetic cloud phase would result in a much less flared Mach cone (see Fatemi 2014). While this cone boundary may still be sonic in nature, it is also garnering features that begin to make it appear quasi-Alfvénic. The flare angle θ also differs by $+4°$ with respect to an angle of $\theta = 20°$ predicted by the model $\theta = \mathrm{atan}(1/M_A)$ for waves in a super-Alfénic flow with a perpendicular IMF and discussed by Zhang et al. (2016). The discrepancy could be due to the magnetic field not being
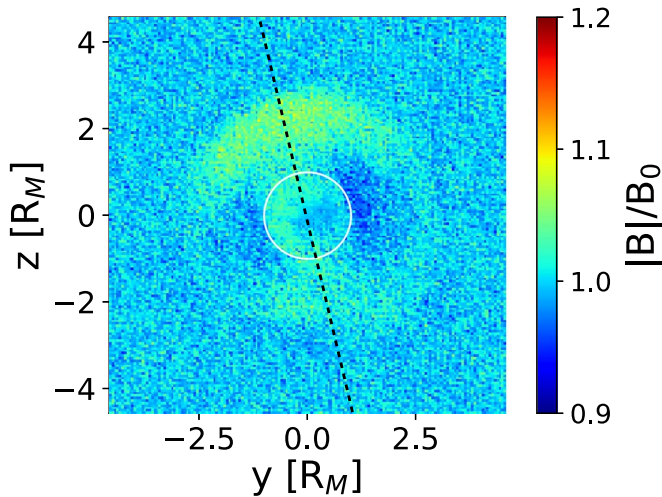
Figure 6. The normalized magnetic field magnitude during the magnetic cloud phase, plotted in the $x = -4 R_M$ plane. The white circle indicates the boundary of the optical wake.

precisely perpendicular to the ambient plasma flow or due to an unknown non-Alfvénic process.

The wake structure also appears as nonsymmetric in the magnetic field in the xz-plane (Figure 4(f)). Figure 6 provides an alternative view of the magnetic field structures during the magnetic cloud phase. The normalized magnetic field magnitude is now plotted in the $x = -4 R_M$ plane, where the white circle indicates the optical wake. Here, it is revealed that the magnetic field structure is generally symmetric about the dashed line in Figure 6. While the magnetic field is more diffuse in the southern ($-z$) region, the slightly angled symmetry further enhanced the appearance of a diffuse southern magnetic lobe in the xz-plane. We also note that the magnetic perturbations from the upstream conditions are relatively low, not exceeding changes of 3 nT.

These characteristics and extreme upstream plasma parameters suggest a very different kind of wake has formed during the magnetic cloud phase. We see a magnetically defined structure that differs from the typical ion sonic wake, but physical mechanisms behind some aspects of the unusual wake structure are still not understood.

All four simulations show a relatively intense and turbulent electric field downstream, but 2D PIC simulations of a lunar obstacle by Kimura & Nakagawa (2008) instead showed intense electric fields at the terminators instead of in the central wake. The strength of these fields more than doubles compared to the ambient upwind field. However, the simulation cell sizes in full PIC models are constrained by the Debye length, which is on the order of a few meters at 1 au. Previous PIC models that are applied to the Moon assume its size to be on the order of 10s of Debye lengths at most (e.g., Birch & Chapman 2001; Kimura & Nakagawa 2008). Their results are likely more representative of a much smaller rocky body—such as an asteroid—and possess similarities to resulting electric fields and particle densities to simulations performed by us using a 2-D treecode on cylindrical obstacles with diameters explicitly defined as 50 and 100 m (not included in this study) and performed by Zimmerman et al. (2014) using an irregular obstacle 200 by 100 m in size (see Figures 2–4 of their study). Due to the small effective obstacle size used by Kimura & Nakagawa (2008), intense downstream electric fields may not have time to form to the extent seen in our results.

Additionally, the intense electric fields at the terminators are likely not physical at full lunar scale. This further supports the hybrid model being very effective at the lunar scale, properly capturing some of the kinetic processes and electric fields that MHD and some simplified particle models cannot capture.

As we show, the CME passage on 2015 June 22 creates sudden upstream plasma changes that alter the wake structure several times during a 24 hr period, only four of which we demonstrate in our simulations. While some CMEs consist simply of a plasma sheath and post-sheath CME phase—such as the CME examined by Farrell et al. (2012)—this event contained multiple magnetic cloud structures following the plasma sheath phase, adding to the dynamic nature of a passing CME. Our hybrid simulations show in detail the plasma void shortening and extending as the plasma sheath and first magnetic cloud pass, in addition to the increased electrostatic turbulence downstream in the wake during the later two phases. Two physical aspects not accounted for in our simulations are proton reflection at the lunar surface by magnetic anomalies and by the photoelectron sheath. At the time of the passing CME, the largest cluster of crustal magnetic anomalies was approximately $45°$ from the Sun–Moon line. The effect of reflected protons by lunar crustal magnetic anomalies is studied by Fatemi et al. (2014) and though their impact is evident, we do not expect the reflected protons to structurally affect the lunar wake. With regard to the photoelectron sheath, observations from the KAGUYA spacecraft show that only 0.1%–1% of the incident protons are reflected from the lunar dayside by the photoelectron sheath, much less than the ∼10% average reflection rate from magnetic anomalies (Saito et al. 2008; Lue et al. 2011).

In this study, we used Wind spacecraft measurements with a hybrid PIC code to model the effect that various phases of a CME have on the lunar plasma wake. Observations showed the arrival of two coherent magnetic structures (magnetic clouds) following the plasma sheath phase, separated by a short period of post-sheath plasma (mid-CME). The results from modeling these phases and the pre-CME phase at the Moon showed a shortened plasma void during the plasma sheath phase that later extended drastically during the magnetic cloud and mid-CME phases. During the magnetic cloud in particular, strong electrostatic turbulence persists further downstream in the wake as the dual ion streams combine. Most interestingly, a flared perturbation in the magnetic field forms during the passing magnetic cloud while no strong sonic rarefaction response is evident. This demonstrates the dynamic way that the lunar wake responds to sudden changes in the upstream solar wind during a CME.

ORCID iDs

Anthony P. Rasca ⓘ https://orcid.org/0000-0002-8816-3693

References

Astafyeva, E., Zakharenkova, I., & Alken, P. 2016, EP&S, 68, 152
Bale, S. D., Kellogg, P. J., Larson, D. E., et al. 1998, GeoRL, 25, 2929
Birch, P. C., & Chapman, S. C. 2001, PhPl, 8, 4551
Burlaga, L., Sittler, E., Mariani, F., et al. 1981, JGR, 86, 6673
Compagnino, A., Romano, P., & Zuccarello, F. 2017, SoPh, 292, 5
Cui, F., & Lei, L. 2008, ChJSS, 28, 189
Farrell, W. M., Halekas, J. S., Killen, R. M., et al. 2012, JGRE, 117, E00K04
Farrell, W. M., Kaiser, M. L., & Steinberg, J. T. 1997, GeoRL, 24, 1135
Farrell, W. M., Kaiser, M. L., Steinberg, J. T., et al. 1998, JGR, 103, 23653
Fatemi, S. 2014, PhD thesis, Luleå Univ. Technology

Fatemi, S., Holmström, M., & Futaana, Y. 2012, JGR, 117, A10105
Fatemi, S., Holmström, M., Futaana, Y., et al. 2013, GeoRL, 40, 17
Fatemi, S., Holmström, M., Futaana, Y., et al. 2014, JGRA, 119, 6095
Fatemi, S., Poirier, N., Holmström, M., et al. 2018, A&A, 614, A132
Fatemi, S., & Poppe, A. R. 2018, GeoRL, 45, 39
Fatemi, S., Poppe, A. R., & Barabash, S. 2020, JGRA, 125, e27706
Fatemi, S., Poppe, A. R., Delroy, G. T., & Farrell, W. M. 2017, JPhCS, 837, 012017
Fuqua Haviland, H., Poppe, A. R., Fatemi, S., et al. 2019, GeoRL, 46, 4151
Garrick-Bethell, I., Poppe, A. R., & Fatemi, S. 2019, GeoRL, 46, 5778
Gopalswamy, N., Mäkelä, P., Akiyama, S., et al. 2018, JASTP, 179, 225
Halekas, J. S., Bale, S. D., Mitchell, D. L., et al. 2005, JGRA, 110, A07222
Halekas, J. S., Saito, Y., Delory, G. T., et al. 2011, P&SS, 59, 1681
Holmström, M., Fatemi, S., Futaana, Y., et al. 2012, EP&S, 64, 237
Kimura, S., & Nakagawa, T. 2008, EP&S, 60, 591
Lue, C., Futaana, Y., Barabash, S., et al. 2011, GeoRL, 38, L03202
Michel, F. C. 2014, JGR, 73, 1533
Nakagawa, T. 2013, JGRA, 118, 1849
Piersanti, M., Alberti, T., Bemporad, A., et al. 2017, SoPh, 292, 169
Poppe, A. R. 2019, JGRA, 124, 6927
Poppe, A. R., Fatemi, S., Halekas, J. S., et al. 2014, GeoRL, 41, 3766
Rasca, A. P., Fatemi, S., Farrell, W. M., et al. 2021, JGRA, 126, e28789
Reiff, P. H., Daou, A. G., Sazykin, S. Y., et al. 2016, GeoRL, 43, 7311
Richardson, I. G., & Cane, H. V. 2010, SoPh, 264, 189
Richardson, I. G., Cliver, E. W., & Cane, H. V. 2001, GeoRL, 28, 2569
Saito, Y., Yokota, S., Tanaka, T., et al. 2008, GeoRL, 35, L24205
Spreiter, J. R., Marsch, M. C., & Summers, A. L. 1970, CosEl, 1, 5
Tao, J. B., Ergun, R. E., Newman, D. L., et al. 2012, JGRA, 114, A03106
Vernisse, Y., Kriegel, H., Wiehle, S., et al. 2013, P&SS, 84, 37
Wang, Y.-C., Müller, J., Ip, W.-H., et al. 2011, Icar, 216, 415
Wolf, R. A. 1968, JGR, 73, 4281
Xie, L. H., Li, L., Zhang, Y. T., et al. 2013, ScChD, 56, 330
Xu, S., Poppe, A. R., Halekas, J. S., et al. 2019, JGRA, 119, 3360
Zhang, H., Khurana, K. K., Kivelson, M. G., et al. 2014, JGRA, 119, 5220
Zhang, H., Khurana, K. K., Kivelson, M. G., et al. 2016, JGRA, 121, 10698
Zhang, H., Khurana, K. K., Zong, Q.-G., et al. 2012, GeoRL, 39, L18104
Zimmerman, M. I., Farrell, W. M., & Poppe, A. R. 2014, Icar, 238, 77
Zimmerman, M. I., Jackson, T. L., Farrell, W. M., et al. 2012, JGRE, 117, E00K03